Direct Torque Control of T-NPC Inverters Fed Double-Stator-Winding PMSM Drives With SVM

***Abstract*—This paper studies and proposes the vector space decomposition (VSD) based direct torque control (DTC) scheme for the T type neutral-point-clamping (T-NPC) three-level inverters fed double-stator-winding PMSM drive, which provides an effective solution for high-power high-reliability applications. The key is to propose a simple but effective space vector modulation (SVM) for DTC of T-NPC double-stator-winding drives based two-step voltage vector synthesis, in such a way that good dynamic response and harmonic performance are obtained. The closed-loop controllers on harmonic subspace are incorporated to suppress the possible harmonics induced from back EMF and unbalanced parameters in phase windings of electrical machine. Furthermore, a hybrid current control is proposed for fault tolerant operation of the T-NPC double-stator-winding PMSM drives under one-phase open-circuit conditions. In the hybrid current controller, the healthy winding still uses the SVM-DTC control while the faulty winding uses the closed-loop current controller to track the optimized current references. Both simulation and experimental results are presented to verify the performance of the proposed switching strategies and control schemes.**

***Index Terms*—Double-stator-winding PMSM drives, T-NPC three-level inverters, vector space decomposition, space vector modulation, fault tolerant control.**

I. INTRODUCTION

With the increasing requirements in power capacity and reliability of some modern industry applications such as high-speed elevators, traction vehicles and electric ships, the electric drives with multiple stator windings are experiencing fast development today [1-4]. When the phase number is multiples of three, the standard “off-the-shelf” power converters can be used. So, the drives with multiple stator windings are regarded preferable for multiphase systems [5]. In order to increase the reliability of the drives, the multiple stator windings could be designed with no magnetic coupling. In such a way, faults in one conversion channel have little impact on operation of other conversion channels. To achieve this goal, multiple three-phase windings can be distributed in well-defined parts of one stator [6]. In particular, the stator permanent-magnet (PM) machines are proposed to achieve magnetic decoupling among different groups of windings by allocating PM magnets and redundant teeth in stators [7-8]. Secondly, the multiple stator windings can also be mounted in multiple stators sharing a common rotor to achieve magnetic decoupling. This multi-stator machine configuration enables the physical separation among multiple stator windings [9-10]. Thirdly, the multiple stator windings can be located in separate motors, whose rotors are coupled mechanically. This multi-motor drive can be applied, where the high-power motor is difficult to realize for strong attractive force of magnet material and heating problem [11].

Normally, the multiple stator windings of the drive are controlled separately, and they are required to track the separate current references to share the total torque of the drive [4, 12]. Recently, intensive research on vector space decomposition (VSD) method have been developed for multiphase drives, where the fundamental components, harmonic components and zero-sequence components are decomposed into orthogonal subspaces respectively [3, 13]. An obvious merit of this method is that the electro-mechanical torque of the drive can be regulated as a whole by controlling components on fundamental subspace, while the harmonic components are limited by optimizing the switching vectors on harmonic component subspace. For further suppressing the low-order harmonics and the unbalanced currents between the multiple windings, additional harmonic current controllers are required on the harmonic current subspace [14-15]. The model predictive control and the decoupling control are proposed based on VSD to achieve fast dynamic performance for multiphase drives [16-17]. The direct torque control (DTC), both the table-based DTC (ST-DTC) and the SVM based DTC schemes have also been proposed for the drives with dual three-phase windings [18]. To suppress the current harmonics, an additional switching table and a flux estimator on $x-y$ plane are added, and a two-step ST-DTC scheme is proposed for the dual three-phase PMSM drives [19]. To avoid increasing complexity of the DTC strategy, new 12 switching vectors are synthesized by voltage vectors from two dodecagons with different amplitudes [20]. To the best of authors' knowledge, all these VSD based control are with two-level inverters fed multiphase drives.

On the other hand, the multilevel inverters fed drives have gained rapid developments recently. The multilevel drives with multiple stator windings incorporate the advantages of both multilevel drives and multiphase drives. They have merits of high equivalent switching frequency, good harmonic performance, low current stress, low common-mode voltage and high fault tolerant capability. So, they provide an effective solution for high-power high-reliability industrial applications, such as electric ship propulsion, turbo-compressor drives, and high-power tractions [21-23]. The VSD field oriented control (FOC) has been proposed for controlling multilevel multiple-stator-windings drives [23-24]. But for the DTC schemes, they are normally used to control multiple three-phase windings separately [25]. To the best of authors' knowledge, the VSD based DTC scheme is still absent for multilevel multiple-stator-winding drives. The reason may lie in the fact that it is hard to design switching logic for DTC from huge number of voltage vectors in multilevel multiple-stator-winding drives [24, 26].

This purpose of this paper is to propose and design the VSD based DTC scheme for T-type neutral-point-clamping (T-NPC) three-level inverters fed double-stator-winding PMSM drives, where the torque generated from multiple stator windings can be controlled as whole. The T-NPC three-level converters inherit the advantages of multilevel inverters such as good harmonic performance, redundant voltage vectors and split DC link capacitors. In addition, the T-NPC three-level inverters have been verified to have small conduction and switching losses although the main switches still withstand the total DC link voltage [27]. Particularly, the T-type three-level inverters are verified to be most efficient during operation with switching frequencies in range of 4-30 kHz compared to two-level inverters and diode neutral-point-clamping (DNPC) three-level inverters [25]. So, the T-NPC

three-level inverters fed double-stator-winding drives are suitable for some low-voltage and high-power applications such as wind energy conversion system, electric elevator drives, and electric vehicle traction systems. To achieve good harmonic performance and well defined switching frequency, the SVM is in adopted in the proposed VSD based DTC scheme. The key is to propose a two-step VSD-SVM strategy, where five groups of original voltage vectors are selected to synthesize harmonic-free acting vectors. It can achieve simple implementation of switching strategy. The mid-point voltage of DC link can be stabilized effectively with redundant vectors by using the proposed modulation. To further suppress the possible harmonics and unbalance, an additional closed-loop current controllers is incorporated to *x-y* subspace, and thus the final switching pattern is generated by adding the voltage perturbation from the controller on *x-y* subspace. The fault tolerant control of T-NPC double-stator-winding PMSM drive is also proposed in this paper, where the SVM-DTC scheme is used in a hybrid way for optimized operation after faults.

The following part of this paper is listed as: The system configuration and modelling are presented in section II. In section III, the detailed principle and design of VSD based DTC scheme is designed and analyzed for the T-NPC double-stator-winding PMSM drives. In section IV, a hybrid fault tolerant control is proposed for the T-NPC double-stator-winding PMSM drives, where the SVM-DTC is kept for the healthy winding. Both simulation and experimental verification are given in section V. Finally, the conclusions are drawn in section VI.

II. Configuration and Modelling

Fig. 1 shows the configuration of the T-NPC double-stator-winding PMSM drive, where a six-phase T-NPC inverter feeds a PMSM drive system with two stator windings. Similar to two-level voltage source inverters, the T-NPC inverters have one switch S_1 in the upper leg, and another one S_4 in the lower leg for each phase. Besides, there are two neutral-point-clamping switches S_2 and S_3, which block half of the DC link voltage. Since the output phase could be clamped to the mid-point of DC link through switches S_2 and S_3, the inverter can output three voltage levels of $+U_{dc}/2$, 0 and $-U_{dc}/2$. The electrical angle between the double three-phase windings could be in-phase, with 30° shifted angle or 60° shifted angle. In this paper, the shifted angle is chosen as 30°, and two neutrals of windings are isolated for eliminating the zero-sequence currents inherently [18].

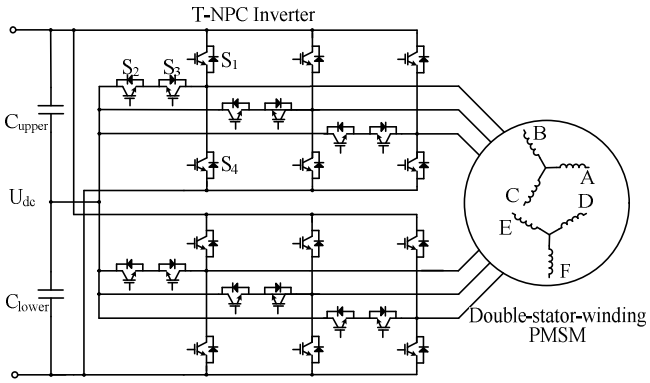

Fig. 1. Configuration of T-NPC double-stator-winding PMSM drive.

The model of double-stator-winding PMSM machine can be simplified by neglecting the magnetic saturation, mutual leakage inductance and core losses while assuming sinusoidal distribution of windings. The voltage and flux models are expressed as:

$$\begin{cases} \boldsymbol{u}_s = R_s \boldsymbol{i}_s + p\boldsymbol{\psi}_s \\ \boldsymbol{\psi}_s = \boldsymbol{L}_s \boldsymbol{i}_s + \boldsymbol{\psi}_f \end{cases} \tag{1}$$

where $\boldsymbol{u}_s = [u_A, u_B, u_C, u_D, u_E, u_F]^T$ is voltage matrix, $\boldsymbol{i}_s = [i_A, i_B, i_C, i_D, i_E, i_F]^T$ is current matrix, and $\boldsymbol{\psi}_s = [\psi_A, \psi_B, \psi_C, \psi_D, \psi_E, \psi_F]^T$ is stator flux matrix. The rotor flux linked to phase windings are $\boldsymbol{\psi}_f = \psi_f [\cos(\theta), \cos(\theta - 2\pi/3), \cos(\theta + 2\pi/3), \cos(\theta - \pi/6), \cos(\theta - 5\pi/6), \cos(\theta + \pi/2)]^T$, where ψ_f is the magnitude of rotor permanent magnet flux and θ is phase angle between the *d*-axis and phase A winding. p is the differential operator and R_s is the stator resistor of each phase. The inductance matrix $\boldsymbol{L}_s$ is given as shown in Eq. (2) [28].

$$\boldsymbol{L}_s = L_{ls}\mathbf{I}_6 + L_{ms}\mathbf{A} - L_{mr}\mathbf{B} \tag{2}$$

where L_{ls} is leakage inductance, L_{ms} is the part of inductance independent of rotor position, and L_{mr} is the part of inductance dependent of rotor position.

$$\mathbf{A} = \begin{bmatrix} 1 & -\frac{1}{2} & -\frac{1}{2} & \frac{\sqrt{3}}{2} & -\frac{\sqrt{3}}{2} & 0 \\ -\frac{1}{2} & 1 & -\frac{1}{2} & 0 & \frac{\sqrt{3}}{2} & -\frac{\sqrt{3}}{2} \\ -\frac{1}{2} & -\frac{1}{2} & 1 & -\frac{\sqrt{3}}{2} & 0 & \frac{\sqrt{3}}{2} \\ \frac{\sqrt{3}}{2} & 0 & -\frac{\sqrt{3}}{2} & 1 & -\frac{1}{2} & -\frac{1}{2} \\ -\frac{\sqrt{3}}{2} & \frac{\sqrt{3}}{2} & 0 & -\frac{1}{2} & 1 & -\frac{1}{2} \\ 0 & -\frac{\sqrt{3}}{2} & \frac{\sqrt{3}}{2} & -\frac{1}{2} & -\frac{1}{2} & 1 \end{bmatrix} \tag{3}$$

$$\mathbf{B} = L_{mr}\begin{bmatrix} \cos(2\theta) & \cos(2\theta - \frac{2\pi}{3}) & \cos(2\theta - \frac{4\pi}{3}) & \cos(2\theta - \frac{\pi}{6}) & \cos(2\theta - \frac{5\pi}{6}) & \cos(2\theta - \frac{3\pi}{2}) \\ \cos(2\theta - \frac{2\pi}{3}) & \cos(2\theta - \frac{4\pi}{3}) & \cos(2\theta) & \cos(2\theta - \frac{5\pi}{6}) & \cos(2\theta - \frac{3\pi}{2}) & \cos(2\theta - \frac{\pi}{6}) \\ \cos(2\theta - \frac{4\pi}{3}) & \cos(2\theta) & \cos(2\theta - \frac{2\pi}{3}) & \cos(2\theta - \frac{3\pi}{2}) & \cos(2\theta - \frac{\pi}{6}) & \cos(2\theta - \frac{5\pi}{6}) \\ \cos(2\theta - \frac{\pi}{6}) & \cos(2\theta - \frac{5\pi}{6}) & \cos(2\theta - \frac{3\pi}{2}) & \cos(2\theta - \frac{\pi}{3}) & \cos(2\theta - \pi) & \cos(2\theta - \frac{5\pi}{3}) \\ \cos(2\theta - \frac{5\pi}{6}) & \cos(2\theta - \frac{3\pi}{2}) & \cos(2\theta - \frac{\pi}{6}) & \cos(2\theta - \pi) & \cos(2\theta - \frac{5\pi}{3}) & \cos(2\theta - \frac{\pi}{3}) \\ \cos(2\theta - \frac{3\pi}{2}) & \cos(2\theta - \frac{\pi}{6}) & \cos(2\theta - \frac{5\pi}{6}) & \cos(2\theta - \frac{5\pi}{3}) & \cos(2\theta - \frac{\pi}{3}) & \cos(2\theta - \pi) \end{bmatrix} \tag{4}$$

The VSD can be used to map the voltage and current space vectors of the double-stator-winding PMSM machine into three two-dimensional orthogonal subspaces, namely α-β, x-y and o_1-o_2. Eq. (5) presents the decomposition matrix of VSD. The α-β subspace comprises fundamental and harmonic components with orders of $6m \pm 5$ (m=1,3,5⋯⋯), and they participate in the electro-mechanical energy conversion. Compared to separate control of multiple three-phase stator windings, the VSD method can control the whole electromagnetic torque of multiple stator windings with current components on α-β subspace. Thus, the possible magnetic coupling among multiple stator windings can be taken into consideration inherently. The components on x-y subspace comprises the harmonic components with orders of $6m \pm 1$ (m=1,3, 5 ⋯⋯). Synthesis of magnetic motive force (MMF) on this subspace is zero, but it introduces major harmonic current due to small impedance on x-y subspace. So, it can be considered as harmonic planes. The components on x-y subspace do not contribute to torque generation. But they will produce additional power loss, and they should be suppressed as low as possible. The components on o_1-o_2 subspace correspond to zero-sequence components [13]. They comprise the harmonic components with orders of 6m±3 (m=1,3, 5 ⋯ ⋯). They do not exist in double-stator-winding machine with isolated neutral points.

$$T_{VSD} = \begin{bmatrix} \alpha \\ \beta \\ x \\ y \\ o_1 \\ o_2 \end{bmatrix} = \frac{1}{3} \begin{bmatrix} 1 & -\frac{1}{2} & -\frac{1}{2} & \frac{\sqrt{3}}{2} & -\frac{\sqrt{3}}{2} & 0 \\ 0 & \frac{\sqrt{3}}{2} & -\frac{\sqrt{3}}{2} & \frac{1}{2} & \frac{1}{2} & -1 \\ 1 & -\frac{1}{2} & -\frac{1}{2} & -\frac{\sqrt{3}}{2} & \frac{\sqrt{3}}{2} & 0 \\ 0 & -\frac{\sqrt{3}}{2} & \frac{\sqrt{3}}{2} & \frac{1}{2} & \frac{1}{2} & -1 \\ 1 & 1 & 1 & 0 & 0 & 0 \\ 0 & 0 & 0 & 1 & 1 & 1 \end{bmatrix} \tag{5}$$

III. PROPOSED DTC BASED ON VSD

Fig. 2 shows the proposed DTC scheme for the T-NPC double-stator-winding PMSM drive based on a two-step voltage vector synthesis SVM. By using the two-step SVM, the design and implementation of switching and control strategies become more convenient. With the feedback of voltage and current components in α-β subspace, the electromagnetic torque T_e and the stator flux ψ_s are estimated. Based on the stator flux error between the reference value and the estimated one, the voltage reference for DTC control are obtained [29]. With the amplitude V_{ref} and position φ of voltage reference, the switching signals are generated by the two-step SVM at the first stage. Then, the final switching signals are obtained by incorporating the voltage perturbation from the closed-loop current controllers on x-y subspace. The components on x-y subspace might be induced by back EMF and asymmetry of machine winding, which will cause additional loss and unbalance in phase currents. So, the closed-loop control is used to regulate x-y current components to suppress them to be zero. The encoder is used to measure the rotor speed, and the closed-loop

speed controller generates the torque reference T_{e_ref} .

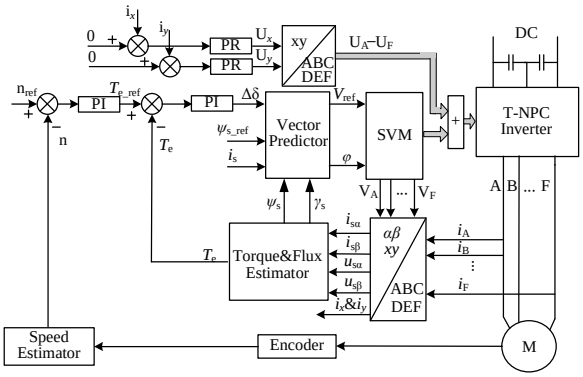

Fig.2. Control diagram of the proposed VSD based DTC for T-NPC three-level inverters fed double-stator-winding PMSM.

A. SVM Based DTC

The amplitude and angle position of the stator flux and torque can be estimated according to the following equations [29]:

$$\begin{cases} \psi_{s\alpha} = \int (U_{s\alpha} - R_s i_{s\alpha})dt \\ \psi_{s\beta} = \int (U_{s\beta} - R_s i_{s\beta})dt \end{cases} \tag{6}$$

$$\gamma_s = arc\tan(\frac{\psi_{s\beta}}{\psi_{s\alpha}}) \tag{7}$$

$$T_e = 3n_p(\psi_{s\alpha} i_{s\beta} - \psi_{s\beta} i_{s\alpha}) \tag{8}$$

where γ_s is the stator flux angle, T_e is the electromagnetic torque and n_p is pole pair number.

As shown in Fig. 3, γ_r is the rotor flux angle. The error of stator flux vector $\Delta\psi_s$ establishes the relation between the stator flux vector and the voltage reference vector V_{ref} as follows:

$$\Delta\psi_s = \psi_{s\_ref} - \psi_s = V_{ref} T_s \tag{9}$$

where ψ_{ref} and ψ_s are stator flux reference and actual stator flux, and T_s is the switching period. Based on the stator flux error, the voltage reference vectors in α-axis and β-axis are obtained in Eq. (10). Therefore, the amplitude V_{ref} and angle position φ of voltage reference vector can be obtained as shown in Eq. (11).

$$\begin{cases} V_{s\alpha\_ref} = \dfrac{\psi_{s\_ref}\cos(\gamma_s + \Delta\delta) - \psi_s \cos(\gamma_s)}{T_s} + R_s i_{s\alpha} \\ V_{s\beta\_ref} = \dfrac{\psi_{s\_ref}\sin(\gamma_s + \Delta\delta) - \psi_s \sin(\gamma_s)}{T_s} + R_s i_{s\beta} \end{cases} \tag{10}$$

$$\begin{cases} V_{ref} = \sqrt{V_{s\alpha\_ref}{}^2 + V_{s\beta\_ref}{}^2} \\ \varphi = \arctan(\dfrac{V_{s\beta\_ref}}{V_{s\alpha\_ref}}) \end{cases} \tag{11}$$

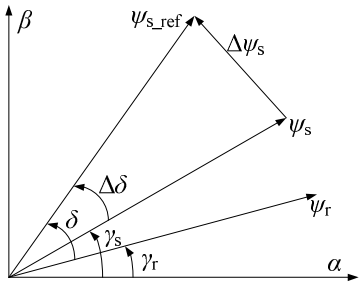

Fig. 3. Phasor diagram of VSD based DTC scheme.

B. SVM Based on Two-step Voltage Vector Synthesis

The voltage references are input to the SVM to generate switching signals. It has been proved that it is the non-zero voltage vectors on *x-y* subspace that produce large harmonics [13]. Therefore, an effective way of reducing current harmonics is to keep the average volt–seconds of voltage vectors on *x-y* subspace zero. In previous literatures, optimized five vector combinations have been proposed for the three-level six-phase drives to achieve the goals [26]. However, a large number of primitive voltage space vectors make the SVM scheme difficult to be implemented. Therefore, a reasonable principle is required to simplify primitive vectors.

Thus, a two-step voltage vector synthesis based SVM scheme is proposed: The first step is to utilize two primitive switching vectors to synthesize the new vectors by forcing the average volt-seconds of voltage vectors on *x-y* subspace to be zero. The second step is to use two synthesized harmonic-free vectors to compose the reference voltage vector. This method can reduce the complexity of SVM scheme and make the design process more convenient. As shown in Fig. 4(a) and Fig. 4(b), the 729 voltage vectors have been mapped into *α-β* subspace and *x-y* subspace for the three-level double-stator-winding PMSM drive. To simplify the voltage synthesis and make more utilization of DC link voltage, only a part of outer primitive vectors are selected to participate voltage vector synthesis process. In Fig. 4, the selected voltage vectors are classified into five groups, according to their amplitudes on *α-β* subspace: L_1, L_2, L_3, L_4, and L_5, which are presented by red, blue, orange, green and purple dots, respectively. The amplitudes of five groups of vectors are listed in Table I.

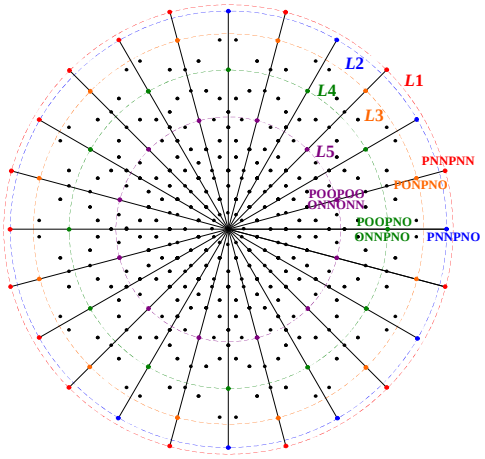

(a)

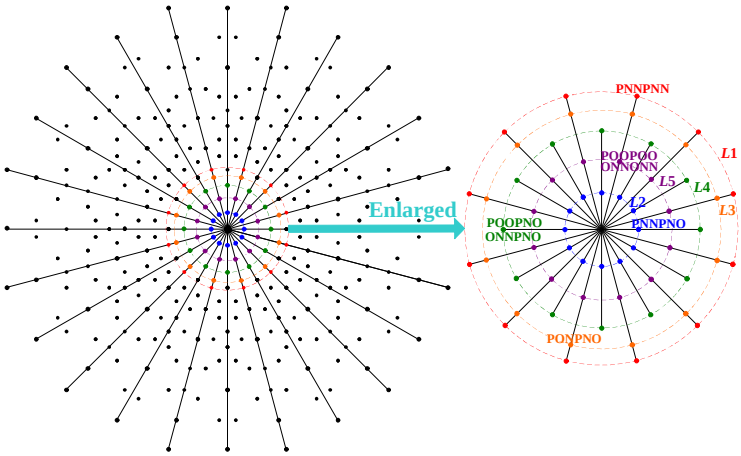

(b)

Fig. 4. Voltage vectors: (a) *α-β* subspace; (b) *x-y* subspace.

TABLE I. AMPLITUDES OF SELECTED VECTORS

	α-β	*x-y*
L_1	$\frac{\sqrt{6}+\sqrt{2}}{6}U_{dc}$	$\frac{\sqrt{6}-\sqrt{2}}{6}U_{dc}$
L_2	$\frac{2+\sqrt{3}}{6}U_{dc}$	$\frac{2-\sqrt{3}}{6}U_{dc}$
L_3	$\frac{3\sqrt{2}+\sqrt{6}}{12}U_{dc}$	$\frac{3\sqrt{2}-\sqrt{6}}{12}U_{dc}$
L_4	$\frac{\sqrt{3}+1}{6}U_{dc}$	$\frac{\sqrt{3}-1}{6}U_{dc}$
L_5	$\frac{\sqrt{6}+\sqrt{2}}{12}U_{dc}$	$\frac{\sqrt{6}-\sqrt{2}}{12}U_{dc}$

According to voltage vectors in Fig. 4, the following relationships are concluded for the five group vectors: First, the vectors in group L_1 and L_3 are with same directions on *α-β* subspace, but they are with opposite directions on *x-y* subspace. For example, PNNPNN of L_1 is with the same direction as PONPNO of L_3 on *α-β* subspace, while they are with opposite directions on *x-y*

subspace. Similarly, the vectors in group L_3 and L_5 are with the same directions on α-β subspace, but they are with opposite directions on x-y subspace. For example, PONPNO of L_3 is with the same direction as POOPOO and ONNONN of L_5 on α-β subspace, while they are with opposite directions on x-y subspace. The vectors in group L_2 and L_4 are with the same directions on α-β subspace, but they are with opposite directions on x-y subspace. For example, PNNPNO of L_2 is with the same direction as POOPNO and ONNPNO of L_4 on α-β subspace, while they are with opposite directions on x-y subspace.

In the first step, the vectors of L_1 and L_3 with same directions on α-β subspace, the vectors of L_3 and L_5 with same directions on α-β subspace and the vectors of L_2 and L_4 with same directions on α-β subspace are selected to synthesize three groups of new vectors, namely $L_{1\text{-}3}$, $L_{3\text{-}5}$, $L_{2\text{-}4}$, respectively. The results are shown in Fig. 5. The constraint of synthesis in the first step is to maintain the average volt-seconds of voltage vectors on x-y subspace to be zero. Thus, the distribution of dwelling time for selected vectors are designed by forcing the components on x-y subspace to be zero according to amplitudes of different layers in Table I. As shown in Table II, $\boldsymbol{PL}_{i\text{-}j(i)}$ and $\boldsymbol{PL}_{i\text{-}j(j)}$ are time weight coefficients of voltage vectors of L_i and L_j, which compose new vectors of group $L_{i\text{-}j}$. The sum of $\boldsymbol{PL}_{i\text{-}j(i)}$ and $\boldsymbol{PL}_{i\text{-}j(j)}$ is one. The amplitudes of three groups of new synthesized vectors are listed in Table III. As shown in Fig. 5, the maximum voltage utilization ratio of the proposed two-step SVM scheme is determined by the amplitude of group $L_{2\text{-}4}$, namely $0.5774U_{dc}$.

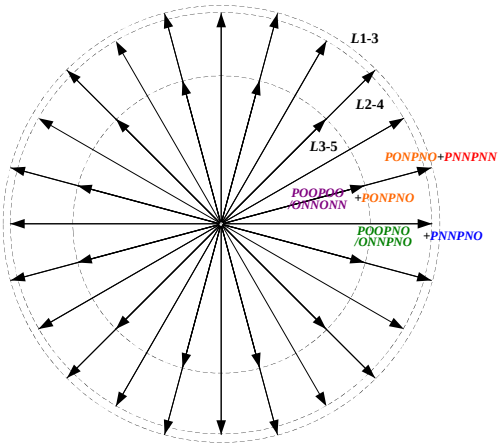

Fig. 5. Synthesized vectors on α-β subspace in the first step.

TABLE II. DISTRIBUTION OF DWELL-TIME OF SELECTED VECTORS

	$\boldsymbol{L_{1\text{-}3}}$	$\boldsymbol{L_{2\text{-}4}}$	$\boldsymbol{L_{3\text{-}5}}$
$\boldsymbol{PL}_{i\text{-}j(i)}$	$2\sqrt{3}-3$	$\frac{-1+\sqrt{3}}{2}$	$\sqrt{3}-1$
$\boldsymbol{PL}_{i\text{-}j(j)}$	$4-2\sqrt{3}$	$\frac{3-\sqrt{3}}{2}$	$2-\sqrt{3}$

TABLE III AMPLITUDES OF NEW SYNTHESIZED VECTORS

	$\boldsymbol{L_{1\text{-}3}}$	$\boldsymbol{L_{2\text{-}4}}$	$\boldsymbol{L_{3\text{-}5}}$
α-β	$\frac{3\sqrt{2}-\sqrt{6}}{3}U_{dc}$	$\frac{\sqrt{3}}{3}U_{dc}$	$\frac{\sqrt{6}}{6}U_{dc}$
x-y	0	0	0

In the second step, the new synthesized 36 vectors are distributed in twelve sectors from I to XII as shown in Fig. 6. Each sector contains four sub-sectors, namely A, B, C and D. Each sector has one zero vector V_1 and five new non-zero vectors V_2 to V_6. The reference voltage vector can be synthesized by three nearest new harmonic-free vectors. For instance, when the reference voltage vector is located in sub-sector I-B, new harmonic-free vectors V_2, V_3 and V_5 participate in the synthesis. According to the volt-second balancing principle, the duration of each new vector can be obtained as:

$$\begin{cases} V_2 T_{V2} + V_3 T_{V3} + V_5 T_{V5} = V_{ref} T_s \\ T_{V2} + T_{V3} + T_{V5} = T_s \end{cases} \tag{12}$$

where V_{ref} is the reference voltage vector, and T_{Vi} is the dwelling time of vector V_i (i=2, 3, 5).

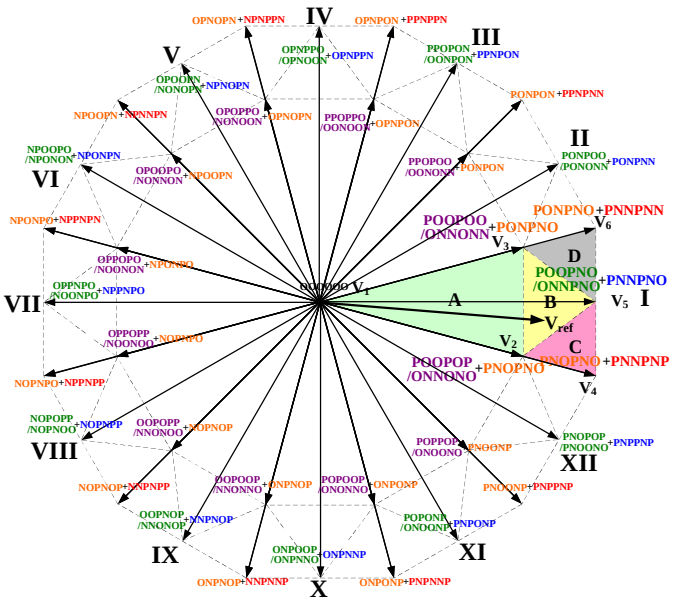

Fig. 6. Principle of two-step voltage vector synthesis SVM.

The redundant voltage vectors are used to suppress the mid-point voltage fluctuation in DC link. The subsector I-B is used for exemplification as following: If the mid-point voltage of DC link is lower than $U_{dc}/2$, the primary voltage vectors POOPOP, PNOPNO, POOPOO, PONPNO, POOPNO and PNNPNO are used. The dwelling time of those primary voltage vectors are calculated by multiplying $PL_{i\text{-}j(i)}$ and $PL_{i\text{-}j(j)}$ to the dwelling time of harmonic-free vectors in the second step. Thus, the values of the dwelling time for the primary voltage vectors are $PL_{3\text{-}5(3)}$ T_{V2}, $PL_{3\text{-}5(5)}T_{V2}$, $PL_{3\text{-}5(3)}T_{V3}$, $PL_{3\text{-}5(5)}T_{V3}$, $PL_{2\text{-}4(2)}T_{V5}$ and $PL_{2\text{-}4(4)}T_{V5}$, respectively. These dwelling time values are expressed as T_1, T_2, T_3, T_4, T_5 and T_6 for simplicity. The sum of the dwelling time for primary voltage vectors is T_s. However, it should be noted that the switching patterns generated by the two-step vector synthesis SVM scheme could not satisfy the requirement that each phase voltage changes only once in a single PWM period. Thus, it is necessary to rearrange the switching sequence based on the volt-second balancing principle. The dwelling time of different voltage levels for each phase are listed in Table IV. The criterion of rearrangement is to concentrate the P level or the N level in the middle while distributing the O level at two sides of the switching period. The total dwelling time of each voltage level in one PWM period is kept unchanged after rearrangement. This switching sequence has lower common-mode voltage since the P level and N level can

cancel with each other in the middle of PWM period. It should be noticed that a short-duration zero vector OOOOOO is inserted at two sides of each switching interval to avoid voltage transition between voltage level P and level N in some phases while switching between different sectors. The constant switching frequency can be maintained by this way. Fig. 7 shows the designed switching patterns when the voltage reference is in sector I and the mid-point voltage of DC link is lower than $U_{dc}/2$.

TABLE IV. DWELLING TIME OF EACH VOLTAGE LEVEL FOR EACH PHASE

	A	B	C	D	E	F
P	T_s	0	0	T_s	0	T_2
O	0	$T_s-T_1-T_5$	$T_1+T_2+T_4$	0	T_2+T_4	T_s-T_2
N	0	T_1+T_5	$T_3+T_5+T_6$	0	$T_s-T_2-T_4$	0

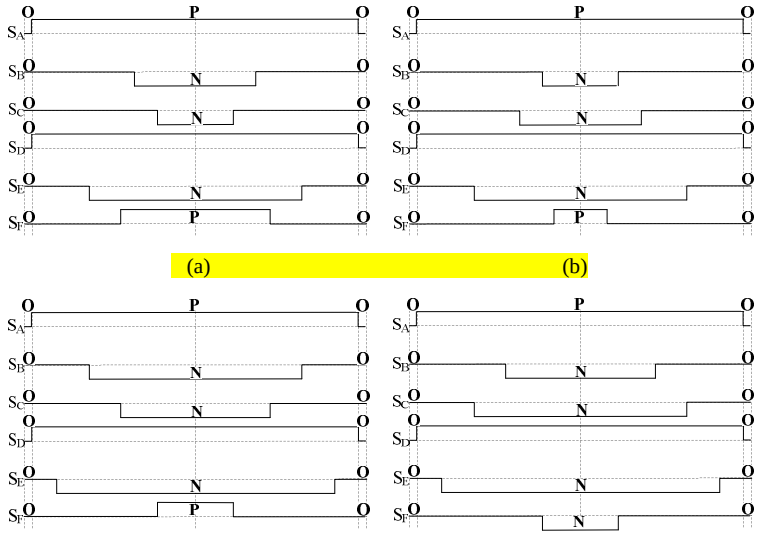

Fig. 7. Switching pattern in sector I after arrangement: (a) subsector A; (b) subsector B; (c) subsector C; (d) subsector D.

C. Current Harmonics Suppression

Although the proposed two-step SVM can limit the harmonics from inverter side, there may be possible current harmonics induced from harmonics in back-EMF and unbalanced parameters in phase windings of electrical machine. In order to compensate the harmonic components, the scheme in this paper introduces a closed-loop controller for harmonic subspace, as shown in Fig 2. The closed-loop harmonic controller generates the voltage perturbation U_x and U_y on *x-y* subspace. With the inverse transform of matrix in Eq. (3), the voltage perturbation on *x-y* subspace are converted into six-phase voltage perturbations, namely $U_A \cdots U_F$. The six-phase voltage perturbations are added to the output voltage of two-step SVM, and produce the final switching signals.

IV. FAULT TOLERANT CONTROL

As aforementioned, the double-stator-winding PMSM drives can offer high fault tolerant capability due to the redundant phase legs. Both the short-circuit and the open-circuit faults can become open-circuit conditions by using fuses or circuit breakers. When the fault occurs, the degraded operation could work by removing the faulty winding completely, and the other healthy winding continues working. Actually, if only one phase is forced open in the faulty winding, the remaining two phases can still produce

torque [13]. In this paper, a hybrid fault tolerant control is proposed for the double-stator-winding PMSM drive under one-phase open conditions. The healthy winding still uses the SVM-DTC control while the faulty winding uses the closed-loop current controller to track the optimized current references under fault tolerant operation. Fig. 8 shows the block diagram of the proposed hybrid fault control scheme for open-circuit fault in phase *D*. The closed-loop speed controller generates the total torque reference T_{e_ref} for the double-stator-winding PMSM machine, and the value will be used for controlling both the healthy three-phase winding and the faulty three-phase winding.

For the faulty windings, two remaining phases *E* and *F* have to carry the currents in opposite directions due to the isolated neutrals of double windings. In order to ensure the maximum torque at given current amplitudes, the current of phase *E* should maintain the same phase as the back-EMF of phases *E* to phase *F*. The back-EMF e_{EF} is expressed as:

$$e_{EF} = \sqrt{3}\omega\psi_f \cos(\theta - \frac{\pi}{6}) \tag{13}$$

Therefore, the current references of phases *E* and *F* can be obtained:

$$i_{E\_ref} = -i_{F\_ref} = I_m \cos(\theta - \frac{\pi}{6}) \tag{14}$$

where I_m is the current amplitude of phase *E* and *F*. In [30], a remedial solution for current references has been proposed by using negative-sequence current components in the healthy winding, so that the minimum copper loss is obtained and sinusoidal current waveforms are maintained. The constraint condition of minimum copper loss is deduced as:

$$I_m = \frac{\sqrt{3}}{2} I_{q\_ref} \tag{15}$$

where I_{q_ref} is the *q*-axis current reference.

Considering the *d*-axis current I_d is zero, the relationship between the electromagnetic torque reference T_{e_ref} and the *q*-axis current reference I_{q_ref} can be expressed as:

$$T_{e\_ref} = 3N_p\psi_f i_{q\_ref} \tag{16}$$

By taking Eqs. (15-16) into Eq. (14), the optimized current references of the faulty winding are deduced as:

$$i_{E\_ref} = -i_{F\_ref} = \frac{\sqrt{3}}{2} I_{q\_ref} \cos(\theta - \frac{\pi}{6}) = \frac{\sqrt{3}}{6} \frac{T_{e\_ref}}{n_p\psi_f} \cos(\theta - \frac{\pi}{6}) \tag{17}$$

Since phase *E* and phase *F* currents are periodic, the proportional resonant (PR) current controller and the level shifted multi-carrier modulation are used to track the reference values of faulty winding.

On the other hand, the SVM-DTC is still used for the three-phase healthy winding. The torque generated in the healthy winding

has to compensate the torque ripple induced by the faulty winding. But the SVM-DTC scheme has to be modified in Fig. 8. The feedback of currents in healthy winding and faulty winding are used to calculate the stator flux ψ_s and the torque T_e. The calculation of stator flux is shown in Fig. 9, which is developed based on current model [29]. Under open-circuit faults in phase windings, the voltage model based flux calculator is difficult to implement since the terminal voltage of faulty winding is hard to measure. On the other hand, the current model is convenient to calculate the stator flux even with open-circuit faults in phase windings. The torque is estimated with the same method as that used under normal condition. So, Eq. (8) can still be used to calculate the torque under the faulty condition. By using closed-loop control of the whole torque of drive system, the torque pulsation caused by faulty winding can be compensated well by the healthy three-phase winding in the electrical machine. The synchronous inductances are $L_d = L_{ls} + 3L_{sm} - 3L_{rm}$ and $L_q = L_{ls} + 3L_{sm} + 3L_{rm}$ for electric drives with double stator windings having magnetic coupling, and $L_d = L_{ls} + \frac{3}{2}L_{sm} - \frac{3}{2}L_{rm}$ and $L_q = L_{ls} + \frac{3}{2}L_{sm} + \frac{3}{2}L_{rm}$ for electric drives with double stator windings having no magnetic coupling.

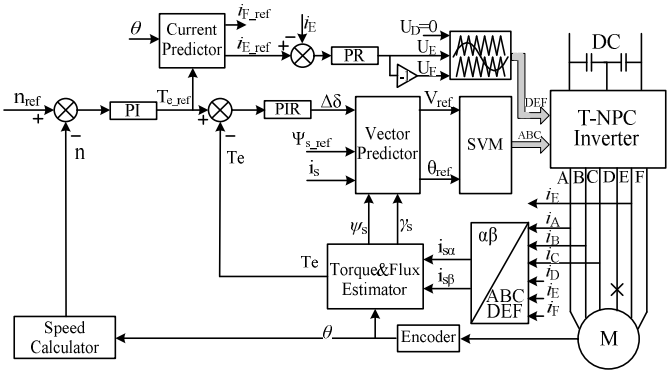

Fig. 8. Block diagram of hybrid fault tolerant control for T-NPC double-stator-winding PMSM drive.

Similar to section III-A, the closed-loop control of torque generates the desired angle deviation $\Delta\delta$. Based on Eqs. (10-11), the voltage references are generated for the healthy three-phase winding. With the three-phase SVM scheme for three-level inverter, the switching signals are generated for the healthy winding. It is noted that the angle deviation $\Delta\delta$ consists of both DC component and periodic components since the healthy winding has to compensate the double-frequency torque pulsation in the faulty winding. So, a resonant control is used together with the PI controller. This hybrid controller could achieve power loss minimization with the fault tolerant control, and also keep SVM-DTC operation for the healthy winding.

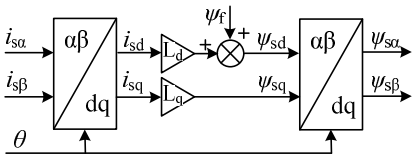

Fig. 9. Calculation of stator flux based on current model.

V. SIMULATION AND EXPERIMENTS

A. Simulation Verification

At first, the MATLAB/Simulink is used to simulate the performance of the T-NPC three-level double-stator-winding PMSM drive. In the simulation, there is magnetic coupling between double stator windings and there is a 30-degree shifted angle between them. The key parameters of the drive system in simulation are given in Table V. Fig. 10(a)-(c) show the simulated steady-state waveforms under 1400 rpm and 20 Nm. In Fig. 10(a)-(c), five-level phase-to-phase inverter output voltages, steady stator flux trajectory and six-phase currents waveforms are observed. Due to the proposed harmonic-free SVM, the harmonics of stator currents are low. Fig. 10(d)-(h) show the transient performance of drive while the rotor speed is changed between 500 rpm and 1000 rpm. It verifies that the actual torque and speed can track their reference values accurately and quickly. The torque ripple is smaller than 0.3 Nm throughout the process. During the transient process, the harmonic components of currents on *x*-*y* subspace are limited low and the maximum amplitude is below 0.4 A, in Fig. 10(g). The currents on *x*-*y* subspace are calculated from measured stator currents based on Eq. (5). The upper and lower capacitor voltages in DC link are controlled well and the difference in their values is less than 2V in Fig. 10(h) by using the proposed switching strategy.

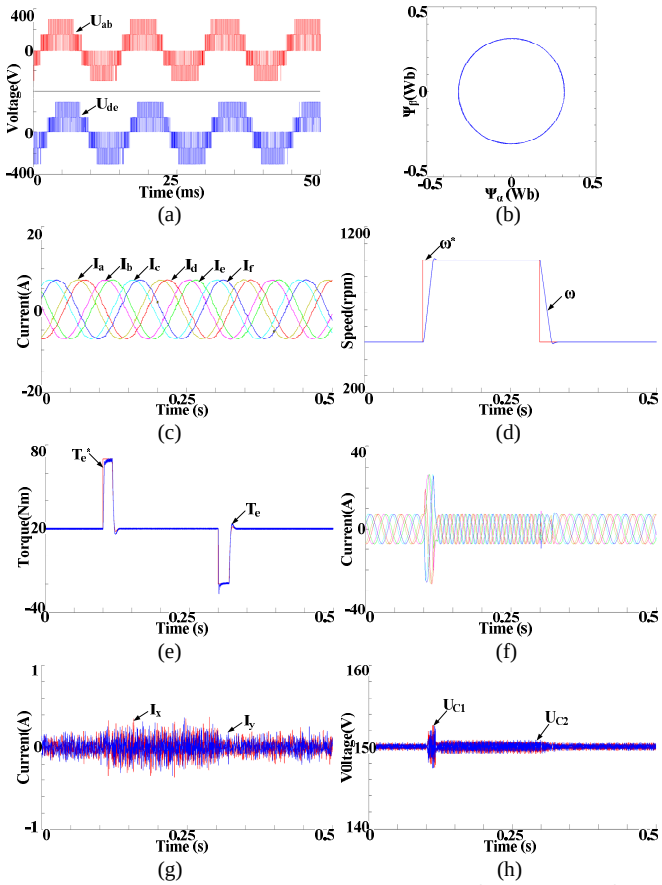

Fig. 10. Simulated performance of drive under normal condition: (a) inverter output voltage waveform; (b) stator flux trajectory; (c) stator currents; (d) rotor speed; (e) torque; (f) stator currents; (g) harmonics on x-y subspace; (h) DC link capacitor voltages.

TABLE V. KEY SYSTEM PARAMETERS.

Name	Simulation	Experiments
Pole pair number n_p	3	3
Stator resistor R_s	0.4 Ω	0.4 Ω
q-axis inductance L_q	16.42 mH	8.71 mH
d-axis inductance L_d	10.36 mH	5.68 mH
PM flux (peak) ψ_f	0.31 Wb	0.31 Wb
DC link capacitor C_{up} , C_{dn}	1000 μF	1000 μF
DC link voltage U_{dc}	300 V	300 V
Switching frequency	5 kHz	5 kHz
Rated speed	1500 rpm	1500 rpm
Rated torque	20 Nm	19 Nm

Fig. 11 shows the effects of the closed-loop controllers on *x-y* subspace for suppressing harmonics from back EMF and asymmetry of machine winding. By adding the 5th order harmonics in back EMF, the obvious current ripples appear in components on *x-y* subspace without the closed-loop controller while the current harmonics are suppressed effectively by incorporating the closed-loop controller in Fig. 11(a). Accordingly, the fifth order harmonics in stator currents induced from back EMF are controlled well in Fig. 11(b). Fig. 11(c) and (d) show that the asymmetrical currents can be controlled balanced with the closed-loop controllers on *x-y* subspace after purposely increasing 1Ω resistor in phase A.

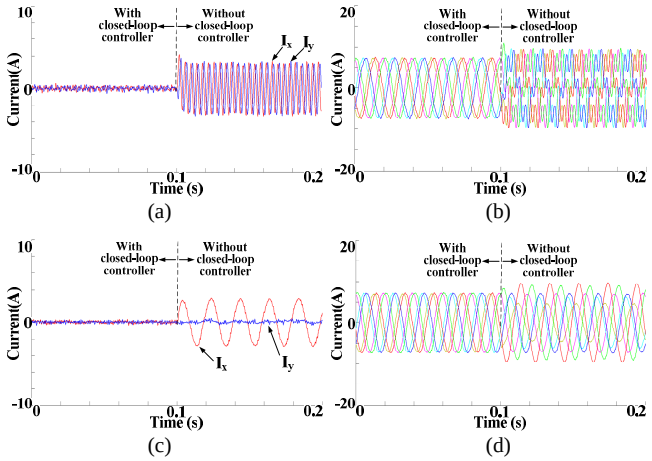

Fig. 11. Simulated performance of closed-loop current controller on x-y subspace: (a) x-y current components with 5th harmonics in back EMF; (b) stator currents with 5th harmonics in back EMF; (c) *x-y* current components with asymmetric resistor in phase A; (d) stator currents with asymmetric resistor in phase A.

Fig. 12 shows the drive performance using SVM-DTC without fault tolerant control when phase *D* is in open-circuit fault. The obvious torque ripple is observed after the fault is introduced in Fig. 12(a) since optimization of torque ripple is not considered in standard SVM-DTC of normal condition. Fig. 12(c) and (d) show the dynamic performance of the drive under *D*-phase open-circuit fault without fault tolerant control scheme. The obvious torque ripple is observed although the upper capacitor voltage and the lower capacitor voltage in DC link are controlled balanced. On the other hand, Fig. 13 shows the drive performance with the proposed fault tolerant control in last section. As shown in Fig. 13(a), the steady-state torque is smooth because the SVM-DTC of healthy winding can compensate the torque oscillation induced from the faulty winding well. The corresponding steady-state current waveforms are shown in Fig. 13(b). Fig. 13(c) and (d) show the dynamic performance of the drive with fault tolerant control

under *D*-phase open-circuit fault. The upper capacitor voltage and the lower capacitor voltage in DC link are controlled well with redundant vectors.

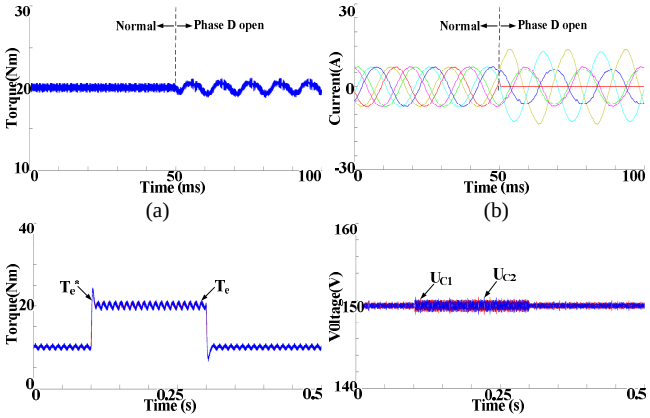

Fig. 12. Simulated performance of drive with standard SVM-DTC under one-phase open-circuit fault: (a) torque; (b) stator currents; (c) torque during transient process; (d) DC link capacitor voltages during transient process.

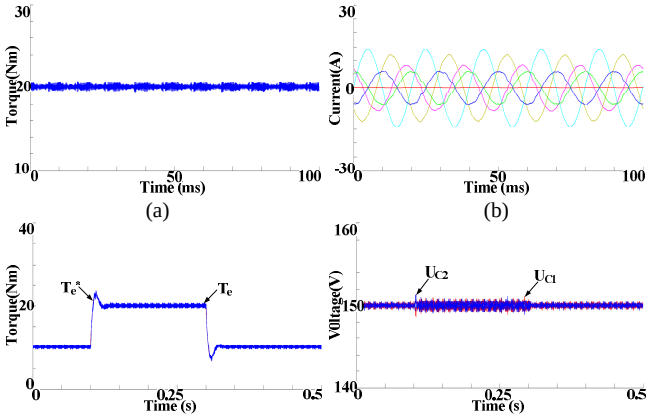

Fig. 13. Simulated performance of drive with proposed fault tolerant control under one-phase open-circuit fault: (a) torque; (b) stator currents; (c) torque during transient process; (d) DC link capacitor voltages during transient process.

B. Experimental Verification

The experiments are carried out on a laboratory prototype of six-phase T-NPC three-level VSI fed double-stator-winding PMSM drive to verify the effectiveness of the proposed control scheme. Fig. 14 shows the photograph of the experimental platform. The detailed system parameters are shown in Table VI. Six power modules (F3L75R12W1H3_B27) are used to build the six-phase legs of T-NPC inverter. The DSP (TMS-F28335) performs the control algorithm and generates the PWM signals. The drivers (M57962L) are used to amplify switching signals for triggering power switches. The LEM-LA25 and LEM-LV25 are used to measure the phase currents and DC link voltages, while the terminal voltages are estimated by switching status and measured DC link voltages. In the experiments, the PMSM drive has double three-phase windings which are magnetically isolated from each other. As mentioned in section I, the double-stator-winding drive without magnetic coupling could be with stators in separate motors, whose rotors are coupled mechanically. A PM generator is used to provide the electric load for the drive.

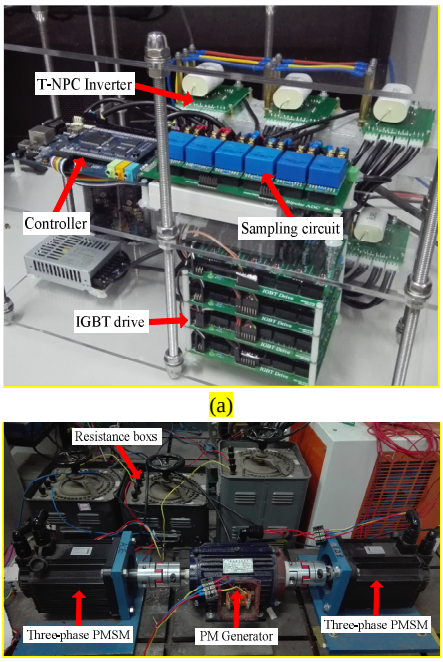

Fig.14. Experimental setup: (a) six-phase T-NPC inverter; (b) electric drive with magnetically isolated double stator windings.

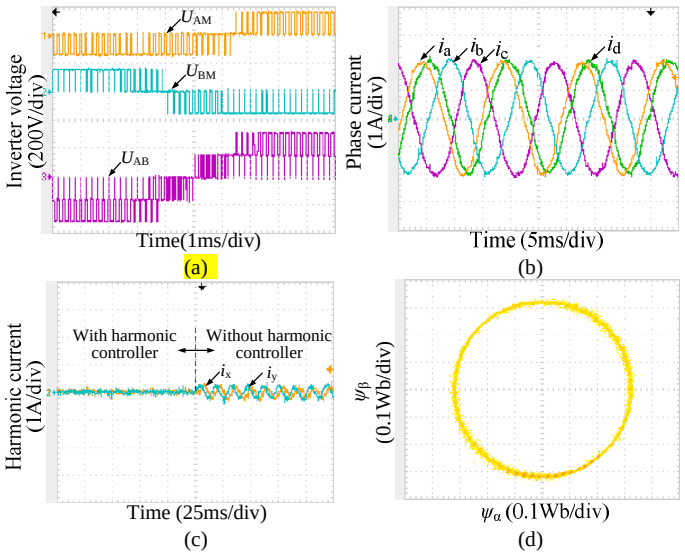

Fig. 15. Measured steady-state performance: (a) inverter voltages; (b) phase current waveforms; (c) harmonic components on *x*-*y* subspace; (d) stator flux trajectory.

Fig. 15 plots the measured steady-state performance of the proposed two-step SVM based DTC control under 1400-rpm 7-Nm condition. Fig. 15(a) shows the three-level phase-to-midpoint voltages (U_{AM} and U_{BM}) and five-level phase-to-phase voltage (U_{AB}) of the inverter. Fig. 15(b) shows the current waveforms of phase windings. It is observed that there is a 30-degree shifted angle between two three-phase windings. Fig. 15(c) shows the harmonic current waveforms on *x*-*y* subspace, where harmonic current ripples appear without the closed-loop harmonic current controller. It could be due to the unbalanced parameters in phase windings of electrical machine. On the other hand, the current components on *x*-*y* subspace can be suppressed effectively with the closed-loop controller on *x*-*y* subspace. Fig. 15(d) plots the measured steady-state stator flux trajectory, and it shows the stator flux

is controlled well.

Fig. 16 shows the comparison of steady-state performance of the drive when different control schemes and modulation strategies are used under 1400-rpm 7-Nm condition. Fig. 16(a) and (b) show the drive performance of two-level operation without and with closed-loop control of harmonic components, respectively. Fig. 16(c) and (d) show the drive performance of three-level operation without and with harmonic components, respectively. The total harmonic distortion (THD) values show that the three-level operation generates less voltage harmonics and current harmonics than the two-level operation. The introduction of harmonic controller can help suppress current components on *x*-*y* subspace. It should be noted that the THD of inverter voltage will increase slightly when the harmonic controller is introduced. It is due to that the closed-loop control of harmonic currents will produce harmonics in inverter voltages.

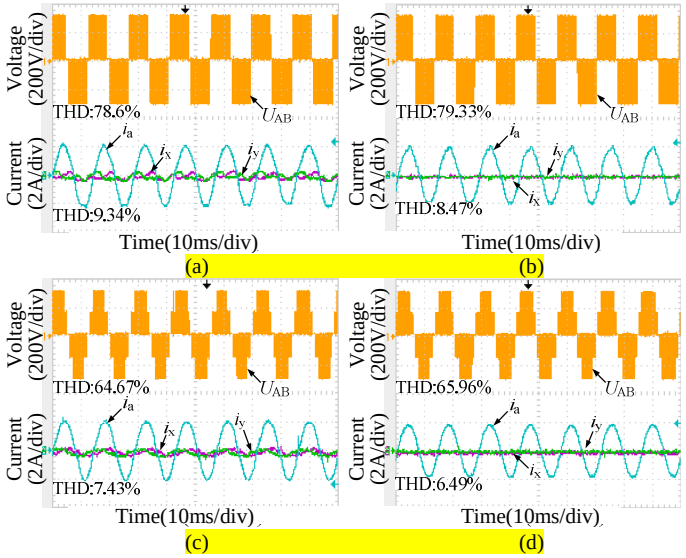

Fig. 16. Harmonic performance: (a) two-level operation without harmonic controller; (b) two-level operation with harmonic controller; (c) three-level operation without harmonic controller; (d) three-level operation with harmonic controller.

Then, the dynamic performance of the drive is measured as shown in Fig. 17 and Fig. 18. Fig. 17(a) shows the measured speed response when the speed is changed between 500 rpm and 1000 rpm. The load torque remains 7 Nm. The fast and accurate tracking performance can be observed for the rotor speed and torque. The torque reference is limited between −40 Nm and 40 Nm. Fig. 17(b)-(d) show the enlarged waveforms during the transient process. In particular, the upper and the lower DC link voltages are controlled balanced in Fig. 17(d). It should be mentioned that the slight dip in the upper and the lower capacitor voltages of DC link are caused by dip of the total DC link voltage during fast change of speed. But the difference between the upper capacitor voltage and the lower capacitor voltage in DC link, namely ΔU_c is suppressed below 6V. Fig. 18 shows the dynamic performance of the drive under transient change in load. The operating speed is kept as 1000 rpm, and the load torque is increased suddenly. It is noticed that the actual torque tracks the reference value quickly and accurately by using the proposed SVM-DTC scheme, and the torque ripple is smaller than 0.5 Nm during the whole process. Also, the upper and the lower capacitor voltages are controlled

balanced as shown in Fig. 18(d).

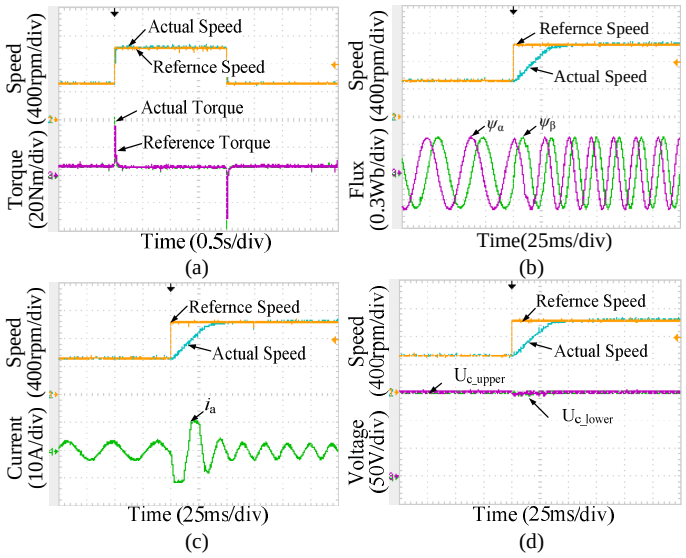

Fig. 17. Measured speed response: (a) speed and torque; (b) stator flux; (c) phase current; (d) upper and lower DC link voltages.

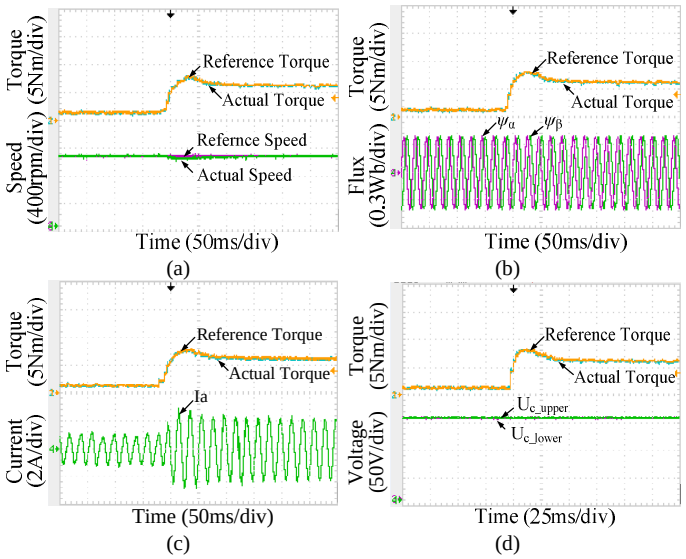

Fig. 18. Measured speed response: (a) speed and torque; (b) stator flux; (c) phase current; (d) upper and lower DC link voltages.

Fig. 19 shows the measured drive performance with standard control of normal condition when phase D is with open-circuit fault. As shown in Fig. 19(a) and (b), phase D current is zero and the remaining two phases E and F have opposite currents after the open-circuit fault in phase D. Fig. 19(c) and (d) show the measured torque and the difference between the upper and the lower capacitor voltages in DC link. Since the standard control scheme is used, obvious torque ripple can be observed after fault under 1000-rpm speed in Fig. 19(c). The difference between the upper and the lower capacitor voltages in DC link, namely ΔU_c is controlled below 4V. by using the redundant vectors in the healthy three-phase winding not only in the steady state of Fig. 19(c) but also in the transient state of Fig. 19(d). Fig. 20 shows the measured drive performance using the proposed fault tolerant control. In Fig. 20(a) and (b), it is noticed that phase D current is zero while phase E and phase F have opposite currents after fault. Fig. 20(c) shows the torque waveforms of two windings, where the torque of faulty winding T_{e2} exhibits the periodic torque ripple. By using

the closed torque controller in Fig. 9, the torque of healthy winding T_{e1} can compensate the torque ripple well, and the torque ripple is decreased from 12.1% to 4.3% of the average torque. The dynamic performance of the drive using fault tolerant control is tested in Fig. 20(d), where load is increased suddenly. The torque can track its reference value accurately while the mid-point voltage of DC link is controlled well.

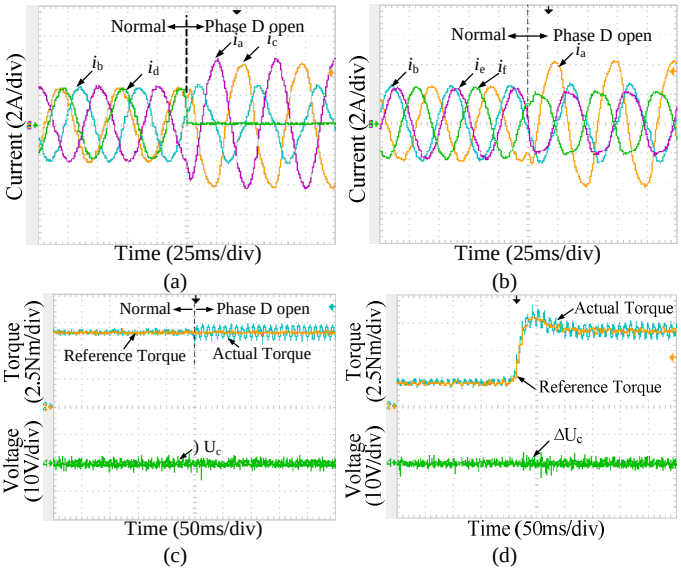

Fig. 19. Measured drive performance under phase D open-circuit fault with standard control: (a) currents of phase A, B, C and D; (b) currents of phase A, B, E and F; (c) torque and mid-point voltage deviation in DC link; (d) performance with load change.

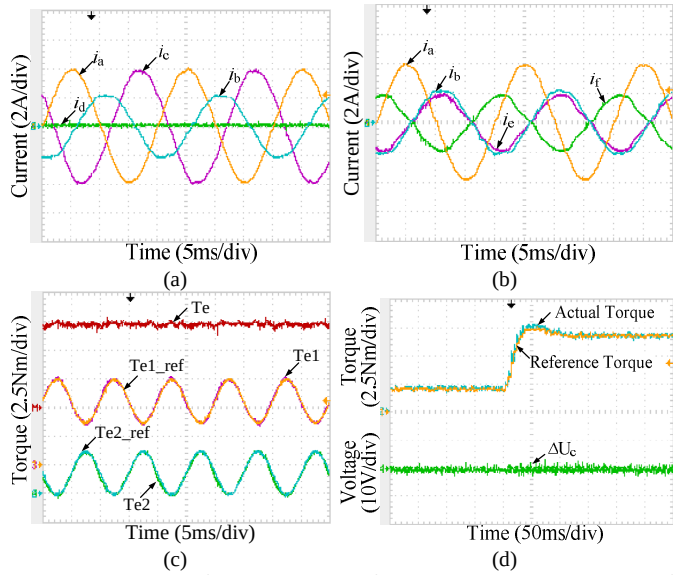

Fig. 20. Measured drive performance under phase D open-circuit fault with proposed fault tolerant control: (a) currents of phase A, B, C and D; (b) currents of phase A, B, E and F; (c) torque; (d) transient performance.

VI. CONCLUSIONS

In this paper, the VSD based DTC control schemes are studied and proposed for T-NPC three-level inverters fed double-stator-winding PMSM drives. To simplify the algorithm and maintain good harmonic performance, a two-step voltage vector synthesis SVM strategy is proposed for the six-phase T-NPC inverters, which is in turn applied for the SVM-DTC scheme.

Three groups of harmonic-free voltage vectors are composed from five original voltage vector groups by forcing their average volt-seconds on *x-y* subspace to be zero. Then, the new three groups of harmonic-free voltage vectors are used in synthesis of final voltage reference. In addition to the merits of easy implementation and elimination of low order harmonics, the proposed two-step voltage vector synthesis based SVM can suppress the mid-point voltage fluctuation in DC link by using redundant voltage vectors. An additional current controller on *x-y* subspace has been designed to generate the perturbation for the switching pulses, which functions to further suppress the harmonics from back EMF and asymmetry of machine winding. To fully utilize high fault tolerant capability of double-stator-winding drives under one-phase open-circuit fault, a hybrid current controller has been proposed in this paper, where the healthy winding still uses the SVM-DTC control while the faulty winding uses the closed-loop current controller to track the optimized current references. Not only the torque ripple can be suppressed under fault conditions, but also the minimum copper loss can be achieved with the optimized current references. The fluctuation of mid-point voltage in DC link is controlled well with redundant voltage vectors of the healthy three-phase winding. The computer simulation is used to verify the control performance of the double-stator-winding PMSM drive with magnetic coupling, and the experiments are applied to verify the control performance of the PMSM drive with two magnetically isolated three-phase windings. Both of them have verified that the proposed switching strategies and control schemes could offer good operating performance under normal and faulty conditions.

REFERENCES

[1] B. Wu, *High-Power Converters and AC Drives*. Piscataway, NJ: Wiley-IEEE Press, 2006.

[2] Kouro, J. Rodriguez, B. Wu, S. Bernet and M. Perez, "Powering the future of industry," *IEEE Industry Applications Magazine*, pp. 26-39, July/August 2012.

[3] E. Levi, R. Bojoi, F. Profumo, H. A. Toliyat and S. Williamson, "Multiphase induction motor drives - a technology status review," *IET Electric Power Applications*, vol. 1, no. 4, pp. 489-516, 2007.

[4] Z. Pan and R. A. Bkayrat, "Modular motor/converter system topology with redundancy for high-speed, high-power motor applications," *IEEE Trans. on Power Electronics*, vol. 25, no. 2, pp. 408-416, February 2010.

[5] L. Alberti and N. Bianchi, "Experimental tests of dual three-phase induction motor under faulty operating condition," *IEEE Trans. on Industrial Electronics*, vol. 59, no. 5, pp. 2041-2048, May 2012.

[6] M. Barcaro, N. Bianchi and F. Magnussen, "Faulty operations of a PM fractional-slot machine with a dual three-phase winding," *IEEE Trans. on Industrial Electronics*, vol. 58, no. 9, pp. 3825-3832, September 2011.

[7] W. Zhao, M. Cheng, K. T. Chau, R. Cao and J. Ji, "Remedial injected-harmonic-current operation of redundant flux-switching permanent-magnet motor drives," *IEEE Trans. on Industrial Electronics*, vol. 60, no. 1, pp. 151-159, January 2013.

[8] M. Cheng, W. Hua, J. Zhang and W. Zhao, "Overview of stator-permanent magnet brushless machines," *IEEE Trans. on Industrial Electronics*, vol. 58, no. 11, pp. 5087-5101, November 2011.

[9] Y. Li, D. Bobba and B. Sarlioglu, "Design and performance characterization of a novel low-pole dual-stator flux-switching permanent magnet machine for traction application," *IEEE Trans. on Industry Applications*, vol. PP, no. 99, doi: 10.1109/TIA.2016.2558160, 2016.

[10] S. Niu, K. T. Chau, J. Z. Jiang and C. Liu, "Design and control of a new double-stator cup-rotor permanent-magnet machine for wind power generation," *IEEE Trans. on Magnetics*, vol. 43, no. 6, pp. 2501-2503, June 2007.

[11] S. K. Tseng, T. H. Liu, J. W. Hsu, L. R. Ramelan and E. Firmansyah, “Implementation of online maximum efficiency tracking control for a dual-motor drive system,” *IET Electric Power Applications*, vol. 9, no. 7, pp. 449-458, 2015.

[12] M. Ali Shamsi-Nejad, B. Nahid-Mobarakeh, S. Pierfederici, and F. Meidody-Tabar, “Fault tolerant and minimum loss control of double-star synchronous machines under open phase conditions,” *IEEE Trans. on Industrial Electronics*, vol. 55, no. 5, pp. 1956-1965, 2008.

[13] Y. Zhao and T. A. Lipo, "Space vector PWM control of dual three-phase induction machine using vector space decomposition," *IEEE Trans. on Industry Applications*, vol. 31, no. 5, pp. 1100-1109, September/October 1995.

[14] H. S. Che, E. Levi, M. Jones, W. P. Hew and N. Abd. Rahim, "Current control methods for an asymmetrical six-phase induction motor drive," *IEEE Trans. on Power Electronics*, vol. 29, no. 1, pp. 407-417, Januray 2014.

[15] Y. Hu, Z. Q. Zhu and K. Liu, "Current control for dual three-phase permanent magnet synchronous motors accounting for current unbalance and harmonics," *IEEE Journal of Emerging and Selected Topics in Power Electronics*, vol. 2, no. 2, pp. 272-284, June 2014.

[16] M. J. Durán, J. Prieto, F. Barrero, and S. Toral, "Predictive current control of dual three-phase drives using restrained search techniques," *IEEE Trans. on Industrial Electronics*, vol. 58, no. 8, pp. 3253-3263, August 2011.

[17] J. Karttunen, S. Kallio, P. Peltoniemi, P. Silventoinen, and O. Pyrhnen, "Decoupled vector control scheme for dual three-phase permanent magnet synchronous machines," *IEEE Trans. on Industrial Electronics*, vol. 61, no. 5, pp. 2185-2196, May 2014.

[18] R. Bojoi, F. Farina, G. Griva, F. Profumo, and A. Tenconi, "Direct torque control for dual three-phase induction motor drives," *IEEE Trans. on Industry Applications*, vol. 41, no. 6, pp. 1627-1636, November /December 2005.

[19] K. D. Hoang, Y. Ren, Z. Q. Zhu, and M. Foster, "Modified switching-table strategy for reduction of current harmonics in direct torque controlled dual-three-phase permanent magnet synchronous machine drives," *IET Electric Power Applications*, vol. 9, no. 1, pp. 10-19, 2015.

[20] Y. Ren and Z. Q. Zhu, "Enhancement of steady-state performance in direct-torque-controlled dual three-phase permanent-magnet synchronous machine drives with modified switching table," *IEEE Trans. on Industrial Electronics*, vol. 62, no. 6, pp. 3338-3350, June 2015.

[21] C. Du, X. Zhang, H. Lin and X. Gao, “Improvement of low-speed operation performance of DTC for three-level inverter-fed multi-phase synchronous motor,” *International Conference on Electrical Machines and Systems*, pp. 132-137, 2005.

[22] A. Tessarolo, G. Zocco, and C. Tonello, “Design and testing of a 45-MW 100-Hz quadruple-star synchronous motor for a liquefied natural gas turbo-compressor drive,” *IEEE Trans. on Industry Applications*, vol. 47, no. 3, pp. 1210-1219, 2011.

[23] S. Bhattacharya, D. Mascarella, G. Joos, J. Cyr, and J. Xu, “A dual three-level T-NPC inverter for high-power traction applications,” *IEEE Journal of Emerging and Selected Topics in Power Electronics*, vol. 4, no. 2, pp. 668-678, June 2016.

[24] Z. Wang, J. Chen and M. Cheng, “Modeling and control of neutral-point-clamping (NPC) three-level inverters fed dual-three phase PMSM drives,” *IEEE Energy Conversion and Congress Exhibition (ECCE)*, pp. 6565-6572, 2015.

[25] M. Schweizer and J. W. Kolar, “Design and implementation of a highly efficient three-level T-type converter for low-voltage applications,” *IEEE Trans. On Power Electronics*, vol. 28, no. 2, pp. 899-907, February 2013.

[26] O. Dordevic, E. Levi and M. Jones, “A vector space decomposition based space vector PWM algorithm for a three-level seven-phase voltage source inverter,” *IEEE Trans. on Power Electronics*, vol. 28, no. 2, pp. 637-649, Feburary 2013.

[27] U. M. Choi, K. B. Lee, and F. Blaabjerg, “Diagnosis and tolerant strategy of an open-switch fault for T-type three-level inverter systems,” *IEEE Trans. on Industry Applications*, vol. 50, no. 1, pp. 495-508, January/February 2014.

[28] S. Kallio, M. Andriollo, A. Tortella, J. Karttunen, “Decoupled d-q model of double-star interior-permanent-magnet synchronous machines,”*IEEE Trans. on Industrial Electronics*, vol. 60, no, pp. 2486-2494, 2013.

[29] D. Swierczynski, M. P. Kazmierkowski, and F. Blaabjerg, “DSP based direct torque control of permanent magnet synchronous motor (PMSM) using space vector modulation (SVM-DTC),” *International Symposium on Industrial Electronics*, pp.723-727, 2002.

[30] Z. Wang, J. Chen and M. Cheng, “Fault tolerant control of double-stator-winding PMSM for open phase operation based on asymmetric current injection,” *International Conference on Electrical Machines and Systems*, pp. 3424-3430, Oct. 22-25, 2014.